https://doi.org/10.5194/essd-2023-341
Preprint. Discussion started: 10 October 2023

A global estimate of monthly vegetation and soil fractions from spatio-temporally adaptive spectral mixture analysis during 2001-2022

Qiangqiang Sun[1], Ping Zhang[2], Xin Jiao[1], Xin Lin[1], Wenkai Duan[3], Su Ma[4], Qidi Pan[1], Lu Chen[1], Yongxiang Zhang[1], Shucheng You[5], Shunxi Liu[6], Jinmin Hao[1], Hong Li[7*], Danfeng Sun[1,8*]

[1]College of Land Science and Technology, China Agricultural University, Beijing, 100193, China
[2]National Geomatics Center of China, Beijing, China.
[3]China Agricultural University Library, China Agricultural University, Beijing, 100193, China
[4]Chinese Research Academy of Environmental Sciences, Beijing, China
[5]Land Satellite Remote Sensing Application Center, Ministry of Natural Resources, Beijing, China
[6]China Land Survey and Planning Institute, Ministry of Natural Resources, Beijing, China
[7]Institute of plant nutrition and resources, Beijing Academy of Agriculture and Forestry Sciences, Beijing, China
[8]Technology innovation Center of land engineering, Ministry of Natural Resources, Beijing, China

Correspondence to: Danfeng Sun (sundf@cau.edu.cn); Hong Li (lih5176@126.com)

https://doi.org/10.5194/essd-2023-341
Preprint. Discussion started: 10 October 2023

Abstract. Multifaceted regime shifts of Earth's surface are ongoing dramatically and—in turn—considerably alter global carbon budget, energy balance and biogeochemical cycles. Sustainably managing terrestrial ecosystems requires an increased understanding of these structurally and functionally heterogeneous multi-component information and their changes, but we remain lack of such records of fractional vegetation and soil information at global scale. Here, we provide a globally comprehensive record of monthly vegetation and soil fractions during the period 2001–2022 using a spatio-temporally adaptive spectral mixture analysis framework. This product is designed to continuously represent Earth's terrestrial surface as a percentage of five physically meaningful vegetation and soil endmembers (photosynthetic vegetation, non-photosynthetic vegetation, bare soil, ice/snow, and dark surface) with high accuracy and low uncertainty, compared to previous vegetation index and vegetation continuous fields product, as well as traditional fully constrained linear spectral mixture models. We also adopt non-parametric seasonal Mann-Kendall tested fractional dynamics to identify shifts based on interactive changes of these fractions. Our results—superior to previous portrayal of the greening planet—not only report a $+9.35\times10^5$ km^2 change of photosynthetic vegetation, but also explore decrease of non-photosynthetic vegetation (-2.19×10^5 km^2), bare soil (-5.14×10^5 km^2), and dark surface (-2.27×10^5 km^2). Besides, Interactive changes of these fractions yield multifaceted regime shifts with important implications, such as a simultaneous increase in PV and NPV in central and southwest China during afforestation activities, an increase of PV in cropland of China and India due to intensive agricultural development, a decrease of PV and increase of BS in tropical zones resulting from deforestation. These advantages highlight that our dataset which provides locally relevant information on multifaceted regime shifts at the required scale, enabling scalable modelling and effective governance of future terrestrial ecosystems. The data about fractional five surface vegetation and soil components are available on Zenodo (https://doi.org/10.5281/zenodo.8323292, https://doi.org/10.5281/zenodo.8331843, Sun, 2023a, b)

https://doi.org/10.5194/essd-2023-341
Preprint. Discussion started: 10 October 2023

1 Introduction

Global terrestrial ecosystems are experiencing rapid and uncertain climate change and anthropogenic impacts since the twenty-first century (Alkama and Cescatti 2016; IPCC 2013; Song et al. 2018), which have profound impacts on shifts of Earth's surface, such as greening of the planet (Chen et al. 2019; Piao et al. 2006; Zhu et al. 2016), afforestation (Chen et al. 2019; Tong et al. 2018), deforestation (Qin et al. 2019; Zeng et al. 2018), agricultural expansion (Chen et al. 2019; Zeng et al. 2018; Yu et al., 2021), glacier melting (Hugonnet et al., 2021; Zemp et al., 2019; Soheb et al., 2022), and urban sprawl (Kuang et al. 2020; Liu et al. 2020; Zhang et al., 2022). These land surface shifts inversely play a fundamental role in affecting climate change via considerably altering the Earth's carbon budget, energy balance and biogeochemical cycles (Lawrence and Vandecar 2015; Qin et al. 2021). Increased understanding of these land cover changes is urgent requirement (Réjou-Méchain et al., 2021; Liu et al., 2020) to support the scientific, legislative and land management communities who strive to understand locally relevant knowledge and further protect, restore, and promote the sustainable use of terrestrial ecosystems under Sustainable Development Goal.

However, land surface interpretation is obstructed by extensive existence of mixed pixels in satellite imagery, especially in heterogeneous landscapes (Roberts et al. 1993). Continuous vegetation indexes (e.g., normalized difference vegetation index, leaf area index) provide limited information on surface composition, which hinders our ability of understanding ecosystem's structurally and functionally multifaceted shifts (Smith et al. 2019; Sun 2015).

Previous advances in spectral mixture analysis method have facilitated investigation of estimating physically fractional vegetation and soil information in the mixed pixels with relatively few field points (Roberts et al. 1993; Small 2004; Smith et al. 1990). These unmixed endmember fractions provide multicomponent time series of information on surface heterogeneous composition and interactive evolution rather than individual vegetation indices (Elmore et al. 2000; Franke et al. 2009; Small and Milesi 2013; Sun 2015) and have been adopted to reveal the temporally dynamical systems under the influence of a changing environment and human (Lewińska et al. 2020; Suess et al. 2018; Sun et al. 2021). Recent studies have proven that spectral mixture analysis model has the advantage of providing more accurate and physically based representation of fraction vegetation-soil continues field in the subpixel level without training samples (Daldegan et al. 2019; Smith et al. 2007). This measurement offers a continuous, quantitative portrayal of land surface properties instead of discrete land cover classes, as well as superior to many of spectral indexes (e.g., vegetation index) (Rogan et al. 2002; Sun et al. 2019; Sun et al. 2020). Despite extensive validation and application of this method at the regional scale, there remain lack of global records of unmixed fractional vegetation and soil information, which may be resulted from the temporal and spatial variability of global intra-class and inter-class endmember spectra (Wang et al. 2021).

Recent advance in endmember variability has verified that Multiple Endmember Spectral Mixture Analysis (MESMA) was recommended be used in most applications considering its robustness in mitigating the endmember variability (Zhang et al., 2019). Such approach is well suited for heterogeneous landscapes because it allows an optimized model with varying the number and types of endmembers within each pixel (Roberts et al. 1998; Franke et al., 2009). However, considering world-wide landscapes with enormous heterogeneity under the climate fluctuations and human activities, the paradox of fine-grained spatial representation and challenged data processing for large scale and long-time series characterization of land surface has not yet been fully solved.

Here, we create a unified monthly fractional vegetation-soil nexuses product for the period 2001 to 2021, with an spatio-temporally adaptive MESMA methods at powerful Google Earth Engine (GEE) platform that provide powerful computational processing to realize planetary-scale analysis of geospatial data, at the same scale as monthly composites of MOD43A4 imageries (500×500m spatial resolution). This product is designed to continuously represent Earth's terrestrial surface as a percentage of surface endmembers with standard endmember spectra globally, providing a gradation of five surface vegetation and soil components: photosynthetic vegetation (PV), non-photosynthetic vegetation (NPV), bare soil (BS), ice/snow (IS), and dark surface (DA). And we use non-parametric seasonal Mann-Kendall test to quantify global trends and their interactive shifts in fractional vegetation-soil nexuses over the full period.

2 Materials and methods

2.1 Dataset

The MCD43A4 Version 6 Nadir Bidirectional Reflectance Distribution Function Adjusted Reflectance (NBAR) product is selected in this study (Schaaf and Wang 2015). Since the view angle effects have been removed from the directional reflectance, this dataset is provided as more stable and consistent daily surface reflectance imageries (bands 1-7) using best representative pixel of 16-day retrieval period of Terra and Aqua spacecrafts at 500-m sinusoidal projection. The MCD43A4 dataset was then temporally aggregated to produce a monthly composited dataset by taking the medium of all valid reflectance in GEE platform during 2001–2022.

The Köppen-Geiger climate classification is a reasonable approach to aggregate complex climate gradients into a simple but ecologically meaningful classification scheme (Beck et al. 2018). This classification scheme includes five main classes and 30 subtypes (Beck et al. 2018). We thus selected recently developed global Köppen-Geiger climate classification maps at a 1-km resolution for the present-day (1980–2016). We initially used the 30-subtype classification for the selection of typical regions for the endmembers collection. Meanwhile, we aggregated 30 sub-types to five main classes (i.e., tropical,

https://doi.org/10.5194/essd-2023-341
Preprint. Discussion started: 10 October 2023

arid, temperate, cold, and polar) according to classification scheme criteria to represent a static climate condition in this study.

The land cover datasets are provided by the collection 6 MODIS land cover products (MCD12Q1) with 500-meter spatial resolution in 2001 and 2022 (Friedl and Sulla-Menashe, 2015). We aggregate the International Geosphere-Biosphere Programme (IGBP) classification types of these datasets into three regions—ecological zone, agricultural zone, urbanized zone. We define ecological zone as combination of evergreen needleleaf forest, evergreen broadleaf forest, deciduous needleleaf forest, deciduous broadleaf forest and mixed forest, closed shrublands, open shrublands, woody savannahs, savannahs, grasslands, permanent wetlands, Permanent snow and ice, barren; refine agricultural zone as aggregation of croplands and mosaics of croplands and natural vegetation; and represent urbanized zone by urban and built-up lands.

2.2 Spatio-temporally adaptive spectral mixture analysis

Recent advances in spectral mixture analysis methods have facilitated investigation of estimating fractional endmember abundances in the mixed pixels (Meyer and Okin 2015; Okin 2007; Roberts et al. 1993). This method assumes that the reflectance of target mixing pixel is a linear combination of the weighting coefficients (proportional endmembers) and associated pure spectra,

$$R_i = \sum_{j=1}^{m} F_j \, E_{i,j} + \varepsilon_i$$

Where R_i is actual reflectance for band *i*; $E_{i,j}$ is the reflectance of a given endmember *j* (1≤*j*≤*m*) for a specific band *i*; *m* is the number of endmembers; F_j is fractional abundance of this endmember j; and ε_i is the residual error for specific band *i*. The fully constrained least squares spectral mixture analysis model, including abundance sum-to-one constraint and abundance non-negativity constraint, is commonly applied for estimation of fractional endmembers to guarantee physically meaningful results (Heinz and Chein-I-Chang 2002). spectral mixture analysis model is assessed by the model residual error (ε_i), reported as the root-mean-square-error (RMSE):

$$RMSE = \sqrt{\frac{\sum_{i=1}^{n} \varepsilon_i^2}{n}}$$

Recent studies have proven that spectral mixture analysis model has the advantage of providing more accurate and physically-based representation of fraction vegetation-soil continues field in the subpixel level without training samples (Daldegan et al. 2019; Smith et al. 2007). The spectral mixture analysis model includes three processes: endmember selection, and fraction estimation, and evaluation.

https://doi.org/10.5194/essd-2023-341
Preprint. Discussion started: 10 October 2023

2.2.1 Nested endmember selection considering spatio-temporal variability.

The quality of spectral mixture analysis is significantly dependent on the representativeness of endmember selected. Endmember spectra used in spectral mixture analysis, in general, can either be derived from measured field spectral library or images (Franke et al. 2009; Sonnentag et al. 2007). The image-based endmember selection method is more practical way because advantage of image endmember is that they can be collected at the same scale as the image and are relatively easy to associate with image features (Rashed et al. 2003). Given that such endmember selection would be hampered by temporal and spatial variability of global intra-class and inter-class endmember spectra, we develop a nested framework for endmember selection considering spatial and temporal variability (Fig. 1).

(1) Recent studies have proposed various compositional endmember frameworks in different application contexts. For example, a framework including substrate, vegetation, dark and ice/snow was proposed and verified globally for both Landsat and MODIS to allow estimated fractions to be compared consistently across diverse climate patterns and land use cover types (Small and Milesi 2013; Sousa and Small 2019). Another framework includes photosynthetic vegetation, non-photosynthetic vegetation, soil, and shade (Roberts et al. 1993), this framework was widely adopted for presentation surface structure across tropical rainforest and dryland systems. Thus, we embody five endmembers to represent surface units, these five endmembers include photosynthetic vegetation (PV), non-photosynthetic vegetation (NPV), bare soil (BS), dark (DA), ice/snow (IS). Concretely, PV refers to green photosynthetic foliage characterized by chlorophyll absorptions in the visible and high reflectance in the near-infrared bands; NPV represents non-tilled cropland/grassland, and tree litters; BS contains soil, rock, and sediment. DA represents a fundamental ambiguity; thus, it may be either absorptive (e.g., black lava), transmissive (e.g., deep clear water) or non-illuminated (shadow) surface. IS is permanent glaciers and snow that are widespread in the polar regions and high mountains.

(2) Considering both climate patterns and land cover types, the typical sites employed for standardized endmembers selection were chosen based on global MODIS sinusoidal grid (10°× 10°intervals). The Köppen-Geiger climate classification zones is adopted as the dominant criterion to undertaking full coverage of climate types (Beck et al. 2018). Meanwhile, we also examine land cover diversity, characterized by Simpson's Diversity Index (D) of annual land use cover data from Terra and Aqua combined MODIS Land Cover Type (MCD12Q1) Version 6 product in 2020 for each MODIS grid.

$$D = 1 - \sum_{i=1}^{m} (P_i)^2$$

https://doi.org/10.5194/essd-2023-341
Preprint. Discussion started: 10 October 2023

Where P_i is percentage of type i land use and cover in the grid, m is number of land use and cover in the grid. Finally, 10 MODIS grids (i.e., h08v05, h12v12, h13v09, h16v01, h21v03, h22v02, h22v08, h24v06, h26v05, h27v06, h29v12) (Fig. S1a), with high land cover diversity (D>0.7, Fig. S1b), and containing all Köppen-Geiger climate types (Fig. S1c), were selected for generation of standardized endmember spectrum.

(3) The representativeness of endmembers always shifts with time variation. A multi-temporal endmembers selection scheme has been validated for various time series images (Sun and Liu 2015; Sun et al. 2018). This process of utilization of both spatially and temporally mixed image collections for endmember selection can consider both spatial and temporal variability. Therefore, the multi-temporal standardized endmembers selection scheme is adopted in 10 typical zones that considering both climate and land cover diversity. Principal component (PC) transformation derived eigenvectors and associated PC images were utilized as criteria for determination of endmember types. Specifically, eigenvector of PC, displaying remarkable differences between shortwave infrared bands with other visible and near-infrared bands, is obviously able to highlight characteristics of IS. While PC eigenvector with relative high contrast between near-infrared band and other bands is mainly dominated by the information of PV, especially in vegetation growing seasons. The BS and NPV will be boosted with the PC when corresponding eigenvector emerges the same direction. Even though there is no obvious regular pattern of eigenvector for DA determination, the PC images can provide adequate information coupled with high-resolution images of Google Earth. After the determination of endmembers type and their PCs in each grid, we ranked these PCs by descending order of the variance contribution, and selected PC images of first three timings for endmember selection. We have listed the endmember types and their highlighting timings for each selected gird in Table S1. The image endmembers can be acquired from the vertex's pixels (200-400 pixels) of scatter plot formed by the PC images at their corresponding timings in each grid. We then exported these acquired pure pixels as regions of interest to compute original MODIS reflectance as endmember spectra.

(4) Besides, we collect MODIS derived endmember spectra used in previous study (Clarke et al. 2013; Daldegan et al. 2019; Meyer and Okin 2015; Sousa and Small 2019). Finally, we establish a library of endmember spectra considering spatio-temporal variability, this library includes 35 GV spectra, 40 BS spectra, 25 NPV spectra, 16 DA spectra, and 15 IS spectra.

(5) To ensure feasibility of pixel-by-pixel operations in GEE, we also consider the similarity between the spectral curves, the hierarchical clustering method is selected to aggregate these spectra of each endmember as sub-groups, and we also calculate average values of sub-groups. Finally, we obtain 4 PV spectra, 4 BS spectra, 3 NPV spectra, 2 DA spectra, and 2 IS spectra to estimate vegetation and soil fractions at global scale during 2001 to 2020 (Fig. 2).

https://doi.org/10.5194/essd-2023-341
Preprint. Discussion started: 10 October 2023

Open Access Earth System Science Data Discussions

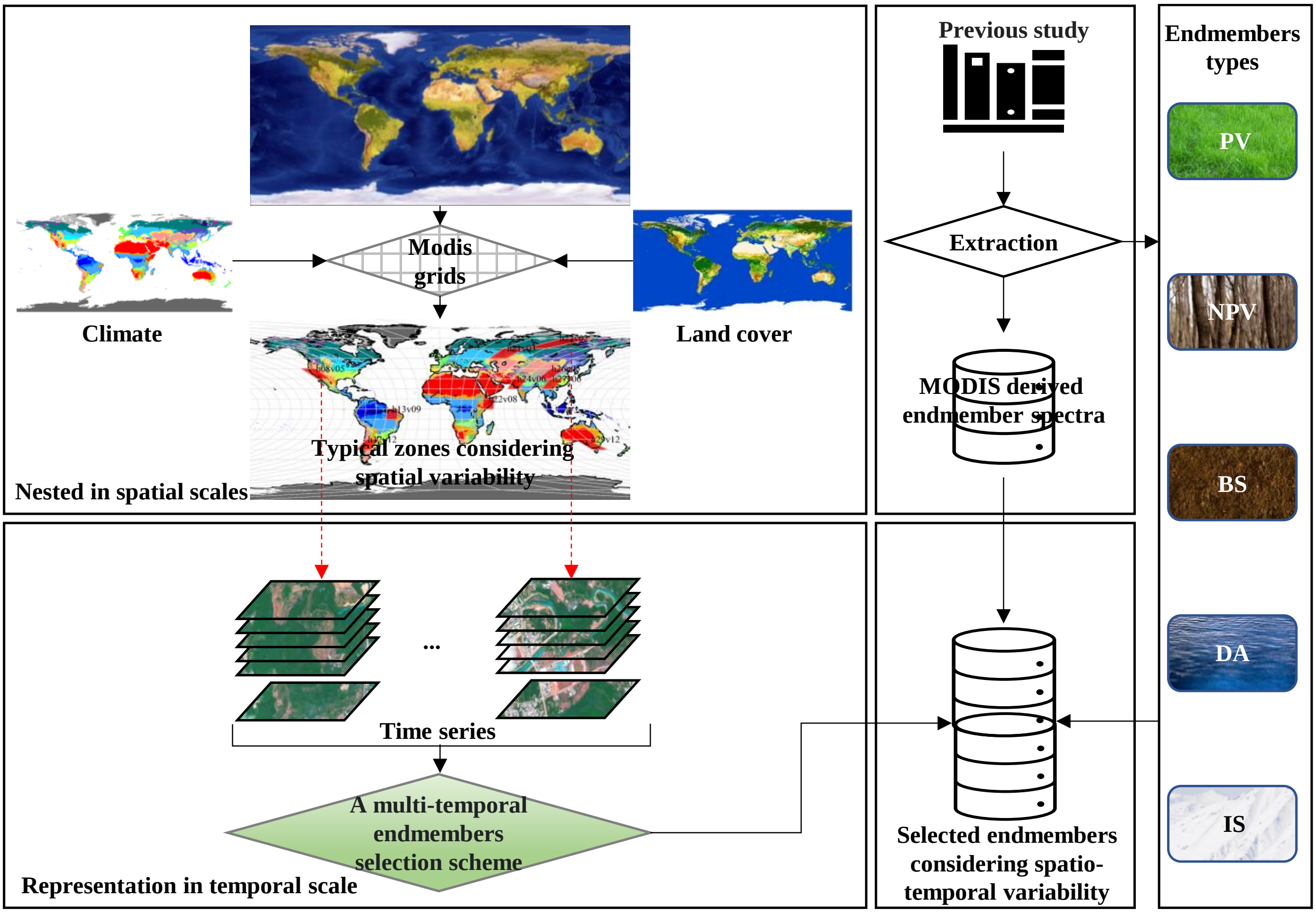

198

199 **Figure 1: A framework for endmember selection considering spatial and temporal variability.**

https://doi.org/10.5194/essd-2023-341
Preprint. Discussion started: 10 October 2023

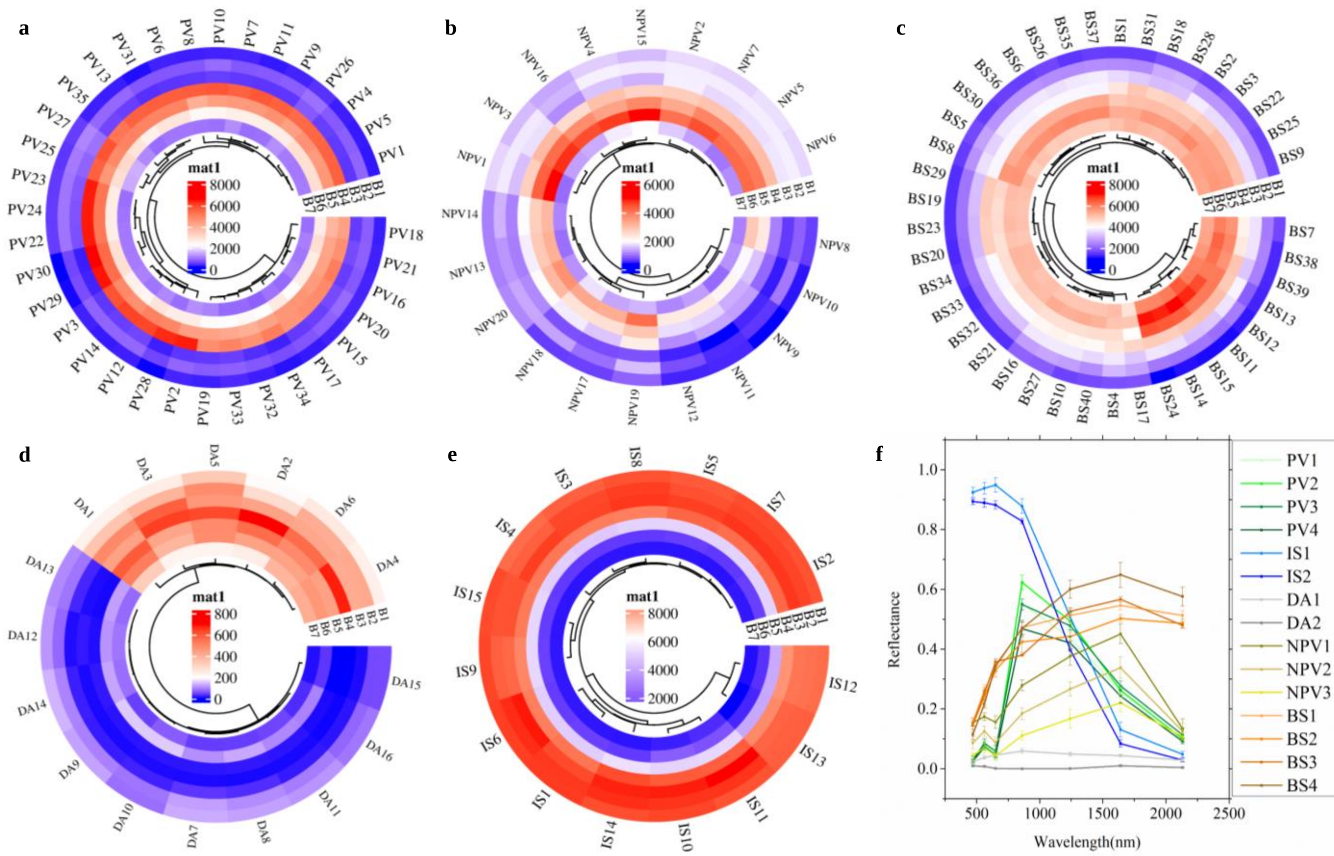

Figure 2: Endmember spectra. a-e, Hierarchical clusters of the endmember spectra of PV, NPV, BS, DA and IS. **f**, the averaged final endmember spectra including 4 PV spectra, 4 BS spectra, 3 NPV spectra, 2 DA spectra, and 2 IS spectra.

2.2.2 Multiple Endmember Spectral Mixture Analysis

The Multiple Endmember Spectral Mixture Analysis (MESMA) has been used to estimate fractional vegetation-soil nexuses based on selected endmember spectra. According to the convex geometry concepts, the number of endmember (n+1) in the model should be equal to the intrinsic dimensionality of the spectral space (n) plus one (Boardman 2013). We found the cumulative contribution of the top three PCs has exceeded 99% (Fig. S2), this three-dimensional PC space allows four-endmember models. We initially generate multiple endmember combinations based on selected endmember spectra, and achieve 692 combination models, including two-endmember model (88), three-endmember model (252) and four-endmember model (352) (Table S2). The fully constrained least squares spectral mixture analysis model is selected to estimate fractions and count RMSE for each endmember combination in GEE platform. We finally search a specific

https://doi.org/10.5194/essd-2023-341
Preprint. Discussion started: 10 October 2023

endmember combination with the smallest RMSE and achieve the estimated endmember fractions of this combination as final fractions.

2.3 Validation of the dataset

The smallest RMSE of 692 combination models is adopted as criteria to assess suitability and uncertainty of the model. The model suggests a generally good fit when mean RMSE over the image is less than 0.02 (Wu and Murray 2003). Moreover, Global Land Cover Validation Reference Dataset (GLCVRD) is provided with a 2m reference dataset from very high resolution commercial remote sensing data within 5 × 5 km blocks in 2010 (Olofsson et al. 2012; Pengra et al. 2015; Stehman et al. 2012). These datasets support global estimates of classification accuracy for four major land cover classes: tree, water, barren, other vegetation, cloud, shadow, ice & snow. Various recent studies have selected this dataset to evaluate the continuous fields of land cover types (Baumann et al. 2018; Qin et al. 2019; Song et al. 2018). We use all GLCVRD reference dataset (Fig. 3a) to assess the accuracy of globally fractional vegetation and soil estimates from MESMA. We exclude those pixels covered by cloud and measured percentage of each land cover type within cloud-free land cover maps (Fig. 3d), and firstly count our generated fractional vegetation and soil estimates within each 5 × 5 km block. PV and NPV endmember fractions are aggregated to match percentage of tree and other vegetation; BS corresponds to barren; DA includes water and shadow, IS refers to ice & snow. Based on paired measured fractions and our estimated fractions within blocks, we adopt four accuracy metrics including mean error (ME), mean absolute error (MAE), root-mean-square-error (RMSE), and R^2 for accuracy assessment.

$$ME = \frac{\sum_{i=1}^{n}(p_i - r_i)}{n}$$

$$MAE = \frac{\sum_{i=1}^{n}|p_i - r_i|}{n}$$

$$RMSE = \sqrt{\frac{\sum_{i=1}^{n}(p_i - r_i)^2}{n}}$$

$$R^2 = 1 - \frac{\sum_{i=1}^{n}(p_i - r_i)^2}{\sum_{i=1}^{n}(p_i - \bar{r})^2}$$

Where p_i, r_i are estimated endmember fractions and reference endmember fractions at ith block, n is sample size (n = 474), $\bar{r}$ is mean of the reference endmember fractions of all blocks.

2.4 Change of vegetation and soil fractions

Mann-Kendall test is commonly referred to as a nonparametric test method, which is procedures that detects monotonic trends of sequences over time (Kendall 1975; Mann 1945). This approach is robustness for trend detection and insensitivity to outliers and provided with an asymptotic relative efficiency of 0.98 relative to the parametric test derived from the coefficient of regression slope (Bradley 1968). When seasonal environmental data of interest are available as time series for which the time intervals between adjacent observations arc less than one year (i.e., daily, weekly, and monthly sequences), the null hypothesis of common Mann-Kendall test may be too restrictive (Hirsch et al. 1982). Therefore, a multivariate extension of the Mann-Kendall test has been advanced to handle seasonal sequences. In addition to identifying the trends of time series records, estimate of magnitude of such a trend is also necessary to quantitatively reveal the change of the time series. The seasonal Sen's slopes (change per unit of time) are commonly chosen to express this magnitude (Hirsch et al. 1982; Sen and Kumar 1968). Therefore, we impose the seasonal Mann-Kendall test and seasonal Sen's method to define trend and slope (annual change) of endmember fractions at the pixel level. The detailed information about seasonal Mann-Kendall test and seasonal Sen's method can be found in Supplementary Methods. If the Mann-Kendall test is not statistically significant ($p \geq 0.05$), we define net change as 0. If the trend test is significant ($p < 0.05$), we apply the seasonal Sen's method to estimate the per-pixel net change between 2001 to 2022 (i.e., slope times 22 years). Besides, we aggregate per-pixel net change of endmember fractions to spatial scales (such as country, biome, climate zone) to obtain total area change estimates at these aggregated scales from 2001-2022 as,

$$\text{Net area change} = \sum_{i=1}^{n} T_i A_i N$$

Where T_i is Sen's slope of endmember fraction for a statistically significant pixel i, A_i represent area of pixel i, n is the total number of such pixels in the region, N is the length of study period ($N = 22$).

3 Results

3.1 Evaluation of monthly estimates of vegetation and soil fractions

We utilize standard endmember spectra globally to estimate fractional vegetation-soil nexuses via MESMA. The simulated results elucidate that the MESMA model performs well with an ideal model RMSE over globe (0.018±0.022, Fig. 3a-c). We find the regions with RMSE above 0.02 account for less than one-fifth of the global area and are mainly distributed in barren such as Sahara Desert and polar regions. This exceptional performance demonstrates the superiority and low uncertainty of the model. This performance is also evidenced by evaluation results from GLCVRD (Fig. 3e-h, Table S3).

https://doi.org/10.5194/essd-2023-341
Preprint. Discussion started: 10 October 2023

Open Access Earth System Science Data Discussions

Specifically, the performance of PV+NPV, BS, and IS endmember estimates is reasonably satisfactory, all of which have MAE less than 0.118, RMSE less than 0.149, R^2 greater than 0.592. Although the MAE (0.050) and RMSE (0.065) perform well, the R^2 of estimated DA against measured DA presents only 0.156. This is resulted from the fact that our estimated DA less than 0.2 is presented as 0 in the reference data, because the interpreted reference dataset of high-spatial satellite observations ignored the shadows of the vegetation. In blocks with a DA greater than 0.2, the estimated DA and measured DA present better consistency, in which the shadows of hills are well measured by GLCVRD.

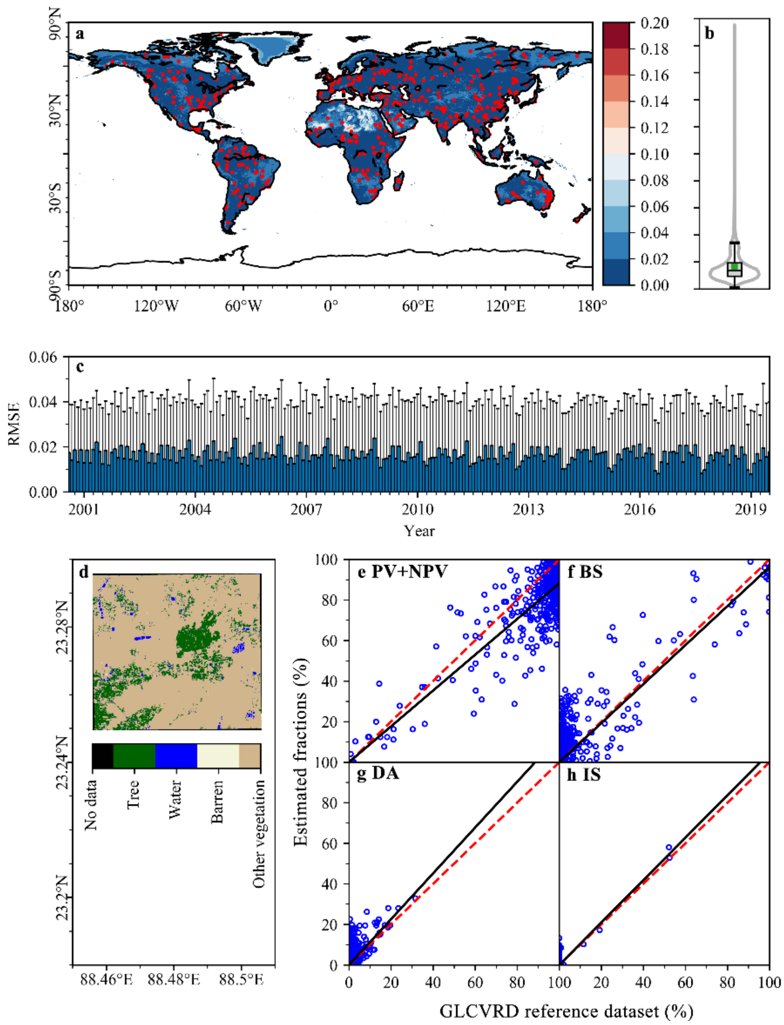

https://doi.org/10.5194/essd-2023-341
Preprint. Discussion started: 10 October 2023

Figure 3: Evaluation of global fractional endmember estimates. **a**, the spatial pattern of average of monthly RMSE from 2001 to 2022, the overlaid red dots were spatial distribution of the 5 × 5 km validation blocks of GLCVRD reference dataset. **b**, the boxplot and violin plot for average of monthly RMSE (a), which indicate mean RMSE over image is less than 0.02. **c**, monthly averaged RMSE from 2001 to 2022 with error bars. **d**, the schematic of detailed land cover classes of GLCVRD reference dataset. **e-h**, Scatter plots of PV+NPV, BS, DA, IS fractions against GLCVRD reference dataset (tree + other vegetation, barren, water + shadow, ice & snow). Endmember fractions were derived from corresponding year and month of each 5 × 5 km block achieved. **i-k**, the bi-dimensional histogram of fractional endmembers and other dataset with bin size of 2%, including fractional PV against NDVI (**i**), fractional PV against LAI (**j**), fractional PV and NPV against fractional tree and non-tree vegetation of MOD44B vegetation continuous fields product (**k**).

3.2 Spatial distribution of global vegetation and soil fractions

Globally averaged monthly gradations of five surface vegetation and soil components are illustrated in Fig. 4. Our estimates depict that PV cover presents the largest area for both 30°-60°N and 0-30°S, which together account for more than half of the total global terrestrial vegetation area. We find the average PV fraction in the Northern Hemisphere is significantly less than that in the Southern Hemisphere, especially in the Amazon, although the area of PV at 30°-60°N is slightly greater than that of 0-30°S. Dominated by foliage-free desert vegetation and agricultural straw, NPV is mainly found in the semi-arid regions (e, g., western China, USA and Australia) and croplands. BS is also located in the drylands of the Sahara, western Asia, and west-central Australia in terms of both fraction and total area. DA and IS, on the one hand, are mainly concentrated in in terrestrial water bodies and mountains, Greenland and global high mountains of the Himalayas and the Andes, respectively.

https://doi.org/10.5194/essd-2023-341
Preprint. Discussion started: 10 October 2023

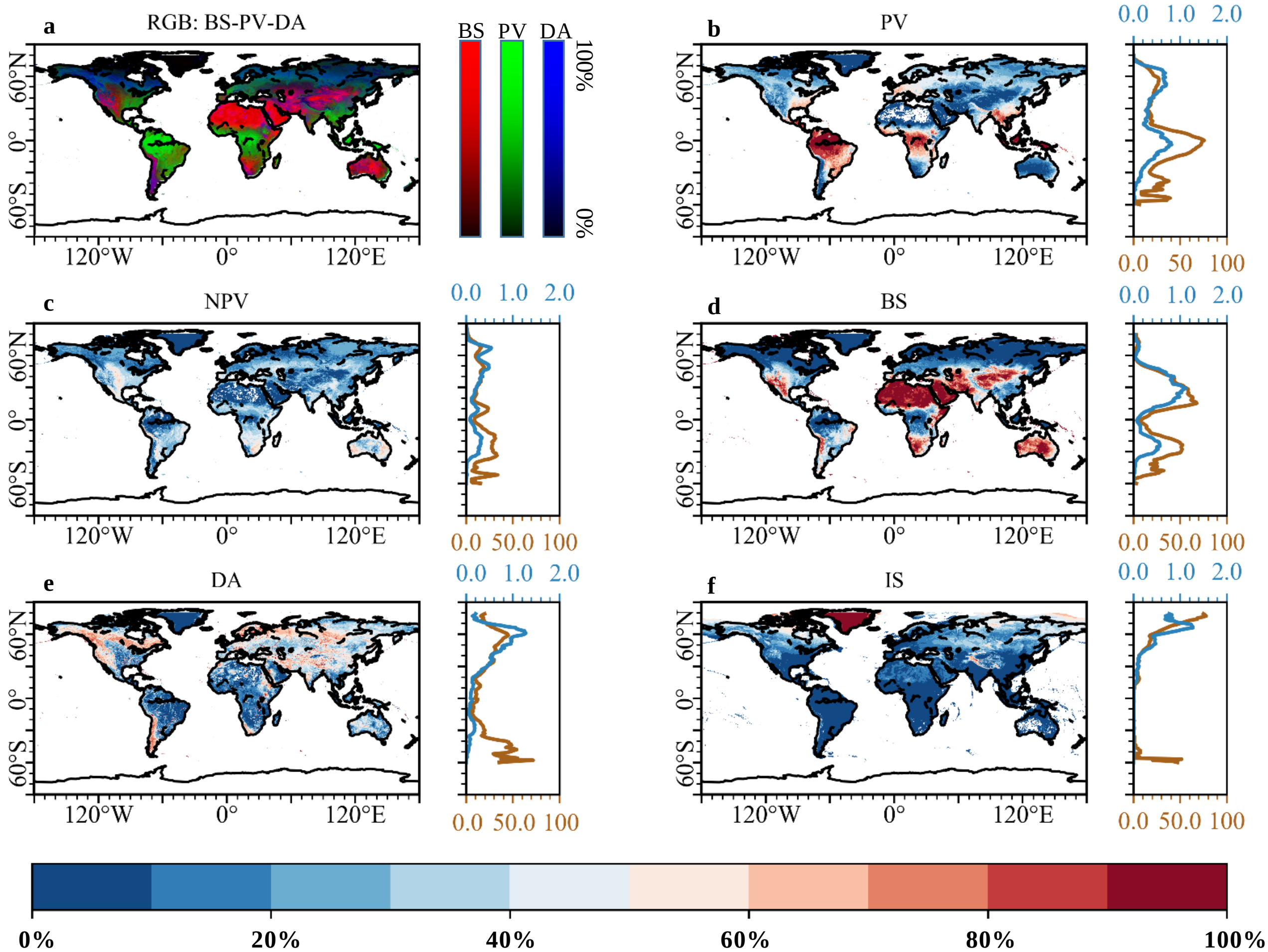

Figure 4: Global average of monthly fractional endmembers from 2001 to 2022. a, Spatialized RGB composition of three averages of monthly fractional endmembers (RGB: BS-PV-DA). b-f, average of PV, NPV, BS, DA, and IS fractions. Shadowed subplots are average of fractional endmembers (%, orange, lower) and area of endmembers (fraction × pixel area, ×106 km2, blue, upper) at respective latitudes, taking each degree as the statistical standard.

3.3 Globally and regionally fractional endmembers dynamics

The total area of PV increases 9.35×10^5 km^2 from 2001 to 2022, which represents a +1.88% change relative to 2001 green vegetation (Fig. 5; Table S4). This increased trend results from higher magnitude of gain (1.57×10^6 km^2), nearly 2.5 times

https://doi.org/10.5194/essd-2023-341
Preprint. Discussion started: 10 October 2023

the loss area. Our PV area gain estimate basically agrees in magnitude with the global vegetation continuous fields product's estimate of net vegetation area change (1.36×10^{6} km^{2}), despite differences in the time period covered (1982-2016) and definition (tree and other vegetation) (Song et al. 2018). Temperate, arid and cold regions together contribute more than 90% of the greening area (Fig. 6; Table S4). In these areas, the China and India are two major contributors (Fig. S3) through land use management like ecological afforestation and agricultural expansion (Chen et al. 2019). Within Brazilian Amazon, we find a large area of PV loss (Fig. S3), which is also supported estimates of forest cover and loss (Qin et al. 2019).

A decreasing trend is observed in NPV globally (2.19×10^{5} km^{2}), representing a -1.45% change relative to 2001 NPV area (Fig. 5; Table S4). Tropical and temperate regions together contribute more than 80% of the loss area of NPV, which may result from global warming induced tree greening. Although the arid is major source of NPV (2.75×10^{6} km^{2} in 2001, 18.2% of globe NPV area), the change area of NPV is only less than 10000 km^{2} (Fig. 6; Table S4).

In the context of the greening of the vegetation, the degree of BS is reduced by 5.14×10^{5} km^{2} during study period, indicating a -1.09% change relative to initial BS of 2001. The decreased global BS trend occurs in temperate, arid and cold regions, accounting over 90% of net BS change area. In contrast, tropical region appears an increasing trend ($+1.22\times10^{5}$ km^{2}), and thus offset the decline in BS in the rest of the regions (Fig. 6; Table S4). This outcome result from the forest loss induced soil exposure in Brazilian Amazon and Southeast Asia (Fig. S3). Meanwhile, the total area of DA also represents a net change of -2.27×10^{5} km^{2}, from 2001 to 2022, which represents a -0.69% change relative to 2001 DA area. The largest negative contributions to the decreased global DA appear in cold (46.26%) and arid (32.87%) (Fig. 6; Table S4). We observed an increase of 2.46×10^{4} km^{2} in IS globally, which represents a +0.11% change relative to 2001 IS. Such positive trend is mainly benefited by the increase of snow and ice in the cold regions, in which the net increase area is 1.5 times greater than the global net IS change (Fig. 6; Table S4). This is caused by the increase of snowfall. However, global warming is causing a substantial melting of snow and ice, resulting in the arid, tropical, temperate and polar regions show a decreasing trend in IS cover.

https://doi.org/10.5194/essd-2023-341
Preprint. Discussion started: 10 October 2023

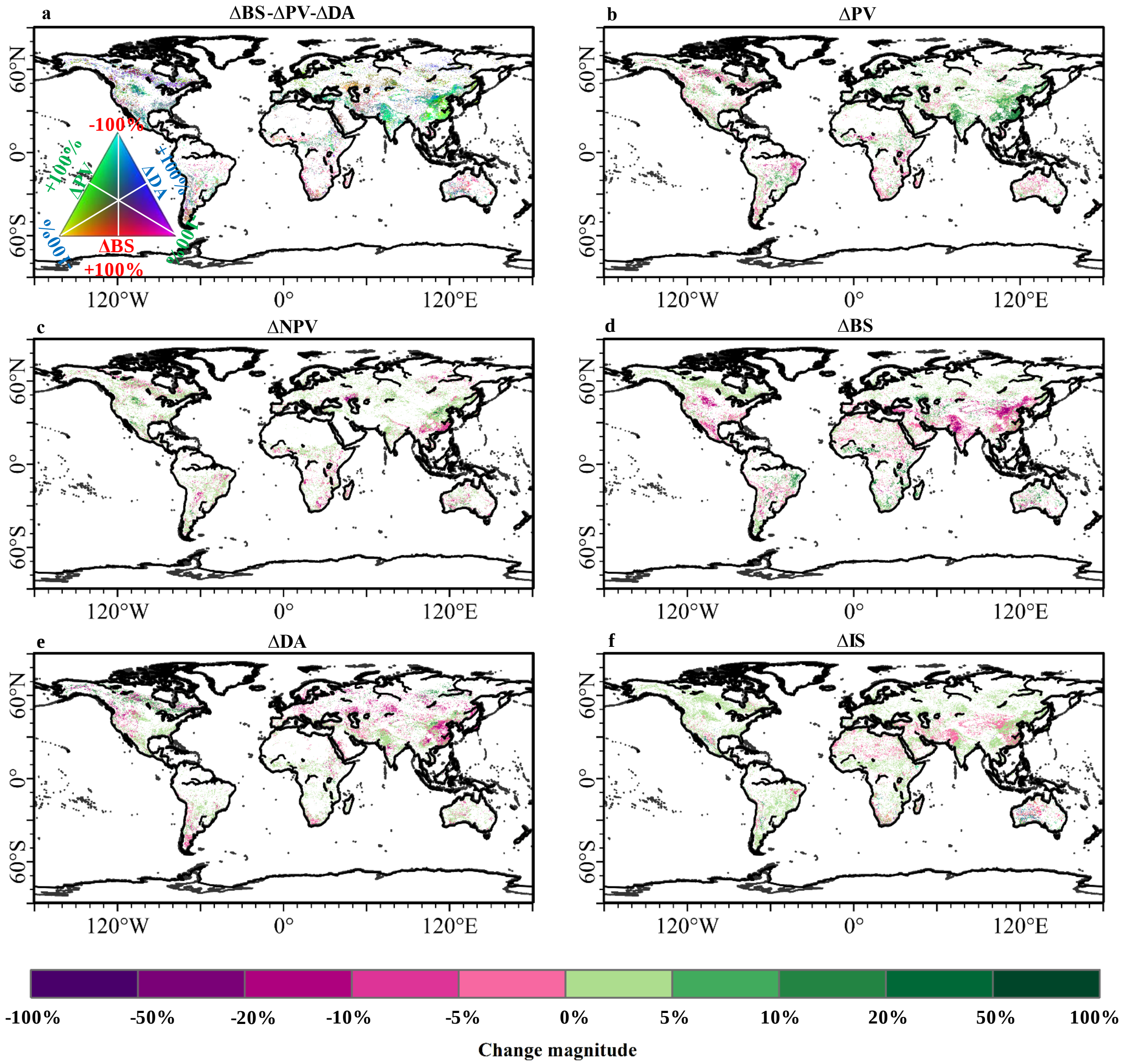

Figure 5: Globally fractional endmembers dynamics at pixel level. a, composited RGB image with ΔBS, ΔPV, and ΔDA. **b-f**, the change magnitude (%) in each pixel for estimated endmembers, i.e., ΔPV, ΔNVP, ΔBS, ΔDA, and ΔIS.

https://doi.org/10.5194/essd-2023-341
Preprint. Discussion started: 10 October 2023

Earth System Science Data
Open Access Discussions

Pixels showing a statistically significant trend (Seasonal Mann–Kendall test, P < 0.05) for either endmember are depicted on the change map.

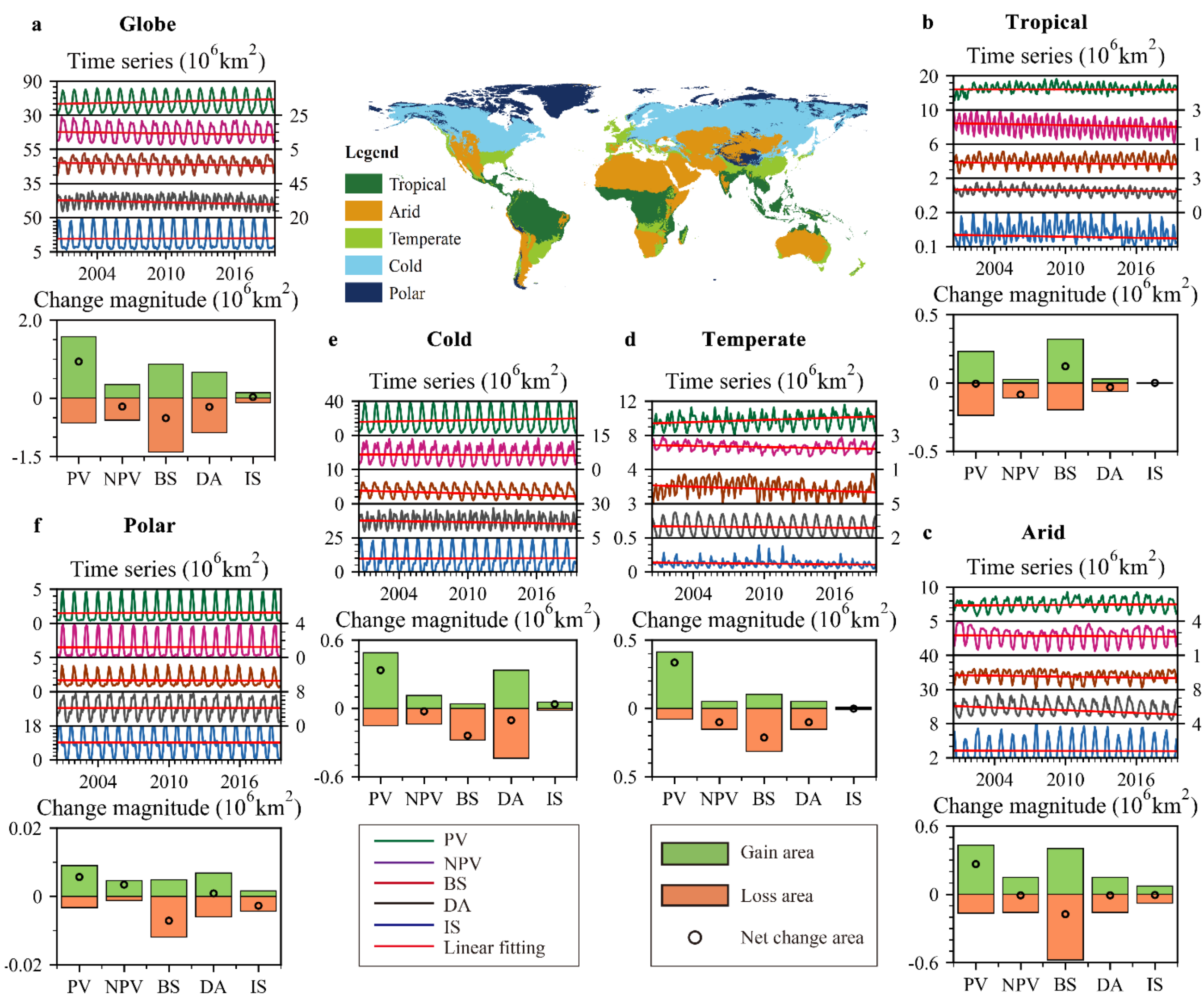

Figure 6: Global and regional fractional endmembers dynamics. The middle subgraph is aggregated five Köppen-Geiger climate classes. **a-f**, the gain area, loss area and net change area for five land surface endmembers in globe (**a**) and five climate zones, i.e., tropical (**b**), arid (**c**), temperate (**d**), cold (**e**), and polar (**f**).

https://doi.org/10.5194/essd-2023-341
Preprint. Discussion started: 10 October 2023

4 Discussions

4.1 Compared with other datasets and traditional SMA model.

We compare our estimates vegetation and soil fractions dataset with NDVI, fractional PV and NPV against fractional tree and non-tree vegetation of MOD44B vegetation continuous fields product (Fig. 7a, b). The PV fractions presents great linear correlations with NDVI and fractional tree and non-tree vegetation (P-value<0.01). However, our product can overcome the problem of saturation of NDVI in the regions embodying high coverage vegetation. Such advance can be supported by previous regional comparison research (Rogan et al. 2002; Sun et al. 2019; Sun et al. 2020). Besides, considering that MOD44B vegetation continuous fields product (DiMiceli et al., 2015) provides a gradation of three surface cover components: percent tree cover, percent non-tree cover, and percent bare, the dark components (i.e., shadow of vegetation and mountain, water) are not quantified. Therefore, fractional PV and NPV is overall biased high, especially in areas with low vegetation cover.

Moreover, we also carry out a comparison with traditional linear spectral mixture analysis to demonstrate the advantages of our spatio-temporally adaptive spectral mixture analysis (Fig.7c, d). Such linear spectral mixture analysis was performed using fully-constrained framework based on two fixed endmember spectral curves: (1) average of all spectral spectra for each endmember and (2) existing spectral spectra from Small and Sousa (2019). Both of two fully constrained linear spectral mixture models are inferior to our framework since we consider the variability of the spectra in both time and space.

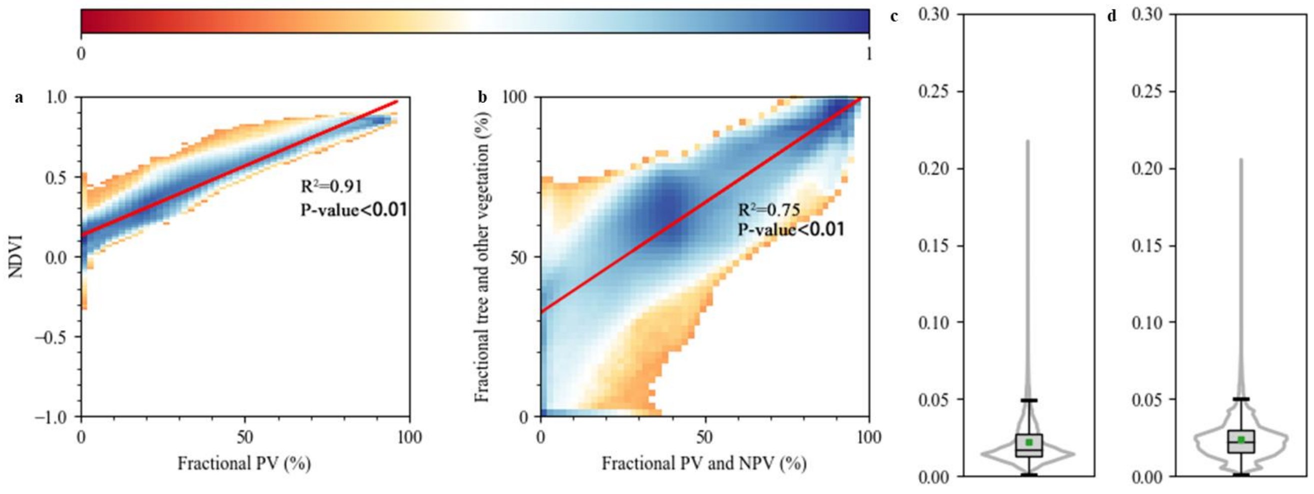

Figure 7: Comparisons with other datasets and LSMA models. a, b, the bi-dimensional histogram of fractional endmembers and other dataset with bin size of 2%, including fractional PV against NDVI (a), fractional PV and NPV

https://doi.org/10.5194/essd-2023-341
Preprint. Discussion started: 10 October 2023

against fractional tree and non-tree vegetation of MOD44B vegetation continuous fields product (b); **c**, **d**, the boxplot and violin plot for average of monthly RMSE for two fixed endmember spectral curves using fully constrained linear spectral mixture models, including (c) average of all spectral spectra for each endmember and (d) existing spectral spectra from Small and Sousa (2019).

4.2 Advances and uncertainties of estimates of global vegetation and soil fractions

This paper implements a globally monthly estimates of fractional vegetation-soil nexuses in 2001–2022 via high-accuracy and time-consuming MESMA algorithm at sub-pixel scale (Roberts et al. 1998), benefited from the GEE platform that can provide powerful computational processing to realize planetary-scale analysis of geospatial data. Moreover, we can more conveniently target the most optimal model from 692 combination models for each MODIS pixel, thus help to understand the specific vegetation-soil compositional structures in each pixel or region (Roberts et al. 1998). Such scheme can improve the ecologists and managers understanding of multifaceted terrestrial ecosystems for differentiated measures. These monthly estimates of fractional vegetation-soil nexuses can be upgraded to multi-timescale (daily, yearly) products to serve different needs, and thus provide multicomponent time series of information on surface heterogeneous composition and interactive evolution. Moreover, these fractional endmembers have been proven their potential for application in land use cover classification (Sun et al., 2020), time-series evolutionary pathways (Sun et al., 2021; Daldegan et al., 2018) and biophysical process modelling (Sun et al., 2022; Sousa and Small, 2018). This globally comprehensive record of monthly vegetation and soil fractions during the period 2001–2022 may provide basic data for quantification and modelling of global change, as well as provide an important foundation for measuring sustainable development goals such as land degradation neutrality (Chasek et al., 2019; Sun et al., 2019).

The temporal and spatial variability of endmembers has always been a significant constraint in obtaining global-scale vegetation and soil fractions from imagery (Wang et al. 2021). The spatio-temporally adaptive framework employed helps to increase the representativeness of endmember selection, and MESMA also considers the suitability of each combination of these endmembers within each pixel. However, considering the limitations of computational resources, our solution on hierarchical clusters of the endmember spectra can improve considerably cost-effective unmixing of long time-series satellite records over globe under the neglect of certain accuracy requirements (Fig. 3). Furthermore, to validate the representativeness of the hierarchical clustering results, we select a spectral spectrum from actually selected endmember spectra that exhibit the largest mean squared error from the mean of cluster for each cluster. These selected spectral spectra were then used to reconstruct an extreme library of endmember spectra and used to estimate fractional vegetation and soil using MESMA. It can be found that 90% of the RESE's differences are concentrated within 1% (Fig. 8a), indicating the relative stability of the unmixed results from two libraries as well as the effectiveness of the clustering. These are also

https://doi.org/10.5194/essd-2023-341
Preprint. Discussion started: 10 October 2023

corroborated by the differences between unmixed endmember fractions (Fig. 8b-e), as indicated by that more than 90% of global pixels have a difference of 10% or less, as well as more than 70% of global pixels present a difference up to 1%, except for the two endmembers with higher spatial variability (NPV, 61.59%; DA, 62.59%). With the assumption of increased computational power in the future, we believe that utilization of combination models from actually selected endmember spectra (35 GV spectra, 40 BS spectra, 25 NPV spectra, 16 DA spectra, and 15 IS spectra) or expanded endmember spectra may further improve the accuracy and stability of estimates of gradations of five surface vegetation and soil components at global scale.

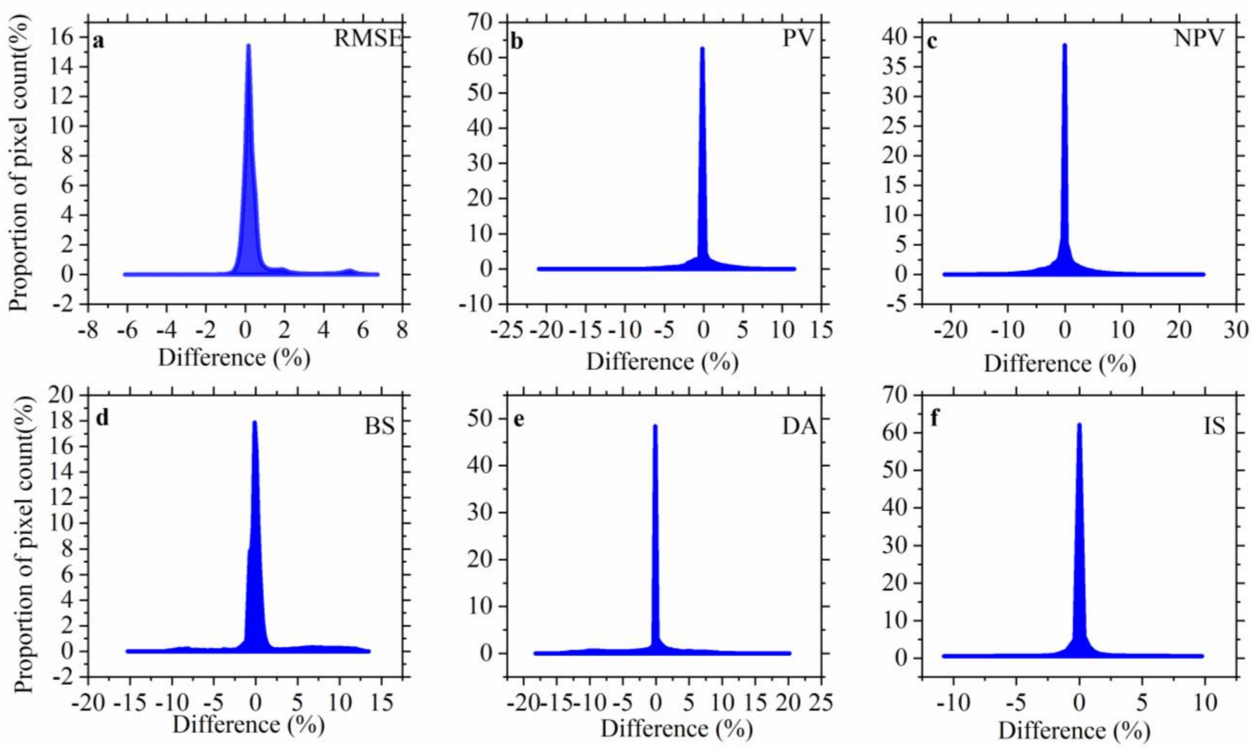

Figure 8: Difference in unmixed results between mean endmember library and endmember library in hierarchical cluster. a, b, c, d, e and f represent histogram of RMSE, PV, NPV, BS, DA and IS.

4.3 Implications of global and regional shifts from pairs of two endmembers

We find greening of Earth characterized by increased photosynthetic vegetation and reduced bare soil exposure, is observed in temperate and cold countries such as China and Russia (Fig. 9; Figure S3). This finding is in agreement with the finding of climate-driven greening trend in Northern Hemisphere (Piao et al. 2006). While the biomass decreases, exhibited as

https://doi.org/10.5194/essd-2023-341
Preprint. Discussion started: 10 October 2023

decreased PV and increased BS (Fig. 9), presented only half of the global climate-driven greening. These findings imply a global trend towards greening in the context of global warming, as supported by a large number of published studies on global vegetation change (Chen et al. 2019; Piao et al. 2006; Song et al. 2018). Moreover, the polar zone is hotspot of ice melting and agrees an accepted fact of accelerated retreat of glaciers and ice under global warming (Hugonnet et al. 2021; Zemp et al. 2019).

Besides, the overexploitation of resources is one of environmental problems of interest and an important factor in causing above climate change and disasters. Global overexploitation has led to problems such as vegetation degradation and intensive utilization of agricultural land. The human overexploitation of forest and grassland induced biomass decrease present a decrease of PV and increase of BS (Fig. 9; Fig. S3), especially over tropical rainforest of Brazilian Amazon and South Asian. This finding agrees with deforestation and agriculturalization in these regions provided by previous studies (Qin et al. 2019; Zeng et al. 2018). Within agricultural area, the agricultural intensification is a human-driven greening process characterized by increased photosynthetic vegetation and reduced bare soil, this shift mainly occurs in India and the North and Northeast China Plain (Fig. 9; Fig. S3) (Chen et al., 2019). We also found urbanization-driven biomass decrease in the global terrestrial ecosystems, especially in China and North America (Fig. 9; Fig. S3), resulted from occupation of agricultural and ecological lands during urban sprawl (Kuang et al., 2020, 2021; Zhao et al., 2022).

Eco-restoration depicts a process that currently needs urgent attention in our understanding and utilization of resources and environment. Different from climate-driven greening that presents trends of increasing PV and decreasing BS, the human-driven afforestation shows positive trends of both PV and NPV, mainly attributed to recent implementing of policies on the ecological restoration through large number of protective forests planted (Fig. 9; Fig. S3). These afforested regions are primarily found over China, Europe, North America, supported by previous study on greening world (Chen et al. 2019). Moreover, Green space construction in urbanized regions has been carried out, integrated with road construction and city renovation, and generate an increasing of footprint of urban greening, especially in China (Fig. 9; Fig. S3).

https://doi.org/10.5194/essd-2023-341
Preprint. Discussion started: 10 October 2023

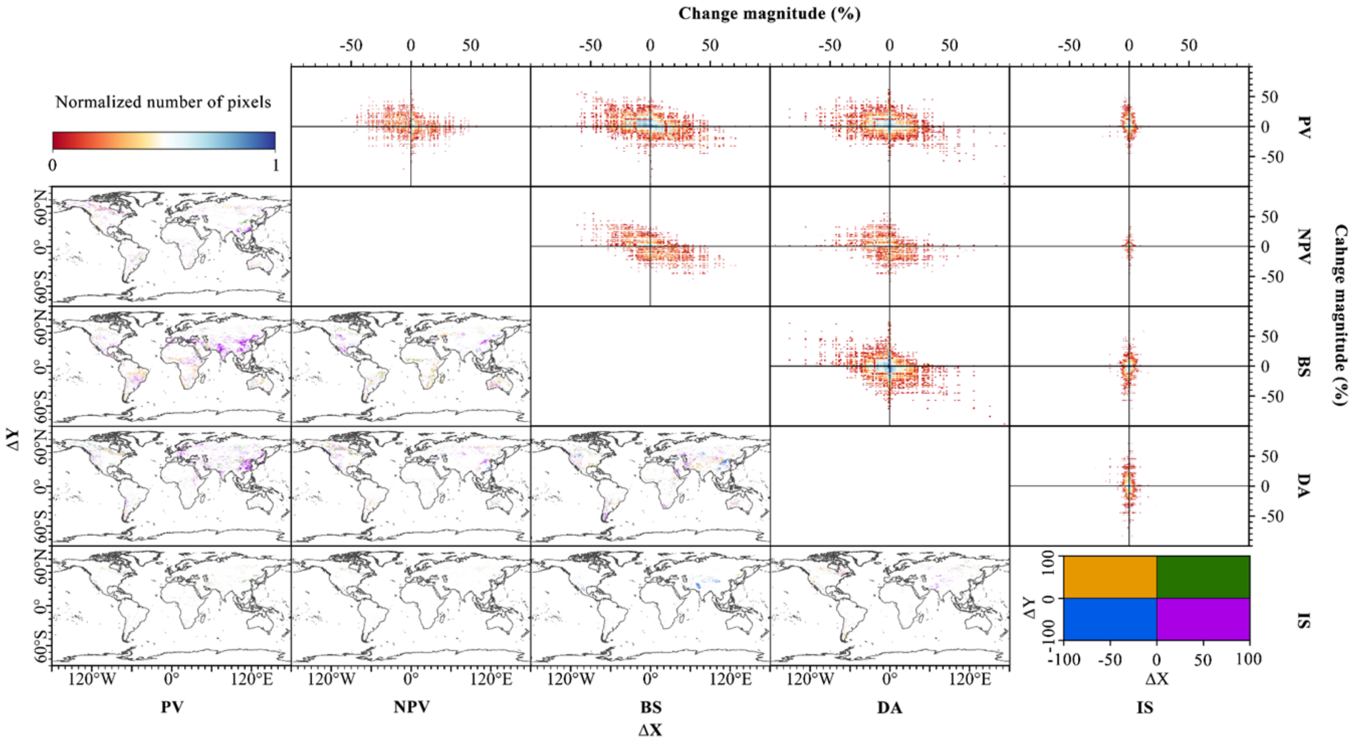

Figure 9: Characteristics of each pair of two endmembers. The bottom left corner was global maps of co-location of paired two endmembers. Pixels showing a statistically significant trend (Seasonal Mann–Kendall test, $P < 0.05$) in both endmembers are depicted on the map. The color of each pixel was displayed in quadrant of ΔX and ΔY, where ΔX and ΔY are horizontal and vertical endmembers, respectively. The top right corner was 2D histogram of change magnitude (%) of paired two endmembers. the x-axes and y-axes were represented by ΔX and ΔY, respectively. These 2D histogram plots were created with bin size of 1% for both axes. The color bar was normalized number of pixels in each bin on a log scale.

5 Data availability

The data about fractional five surface vegetation and soil components can be exported from GEE platform via provided codes or are available on two Zenodo (https://doi.org/10.5281/zenodo.8323292, https://doi.org/10.5281/zenodo.8331843, Sun, 2023a, b). The first dataset includes five fractions from 2001-2011, another includes five fractions from 2012-2022. The file is a compressed month-by-month GeoTIFF data for each year, according to the grid of longitude 60° and Latitude 50°. Since the dataset for each year includes 216 files, named as "SMA_year_(month-1)_gridid.tif", like "SMA_2001_0_0.tif". The public datasets have been listed in the Methods.

6 Code availability

The GEE codes for the MESMA and seasonal Mann-Kendall test will be available at GitHub (https://github.com/qiangsunpingzh/GEE_mesma) or other platforms upon publication; Common code for generating figures is available at https://matplotlib.org/.

7 Conclusions

In this paper, to provide locally detailed socio-ecological knowledge about globally multifaceted changes in fractional vegetation-soil nexuses under climate change and anthropogenic impacts, we estimated monthly vegetation and soil fractions in 2001–2022 that provide multi-component information on surface heterogeneous composition based on a spatio-temporally adaptive spectral mixture analysis framework. This product of monthly vegetation and soil fractions from 692 combination models can provide an accurate estimate of surface heterogeneous composition, better than previous vegetation index and vegetation continuous fields product, as well as traditional fully constrained linear spectral mixture models. This solution can both improve considerably cost-effective unmixing of long time-series satellite records over globe and meet the accuracy requirements. Based on these estimates of vegetation and soil fractions, we find a greening trend of Earth, as indicated by a increase of the total area of PV, which represents a +1.88% change relative to 2001 green vegetation. This greening trend can be found all climatic zones other than the tropics. In addition to the trends in the greening reported by other study, we also found that the increase in PV was accompanied by a decreasing trend in BS, DA and NPV in most regions. And there is a trend of simultaneous increase in PV and NPV in central and southwest China during afforestation activities. Therefore, a combination between interactive changes of vegetation and soil fractions can be adopted as a valuable measurement of climate change and anthropogenic impacts.

Author contributions

Q.S., D.S., P.Z., and H.L. designed the study. Q.S and P.Z. performed the analysis with support from D.S., H.L., J.H., S.L., and S.Y. Q.S., P.Z., and D.S. drafted the paper. Q.S., P.Z., X.J., M.S., F.L., W.D., S.M., A.L., Y.Z., and H.L. collected data and prepared figures. All authors contributed to interpretation of the results and discussions as well as manuscript editing.

Competing interests

The contact author has declared that none of the authors has any competing interests.

Acknowledgements

We thank Bruce W. Pengra for providing the GLCVRD reference dataset.

Financial support

Funding for this work was provided by the National Natural Science Foundation of China (grant nos. 42001234, 42071252).

References

Alkama, R., Cescatti, A.: Biophysical climate impacts of recent changes in global forest cover. Science, 351, 600-604, https://doi.org/10.1126/science.aac8083, 2022.

Baumann, M., Levers, C., Macchi, L., Bluhm, H., Waske, B., Gasparri, N.I., Kuemmerle, T.: Mapping continuous fields of tree and shrub cover across the Gran Chaco using Landsat 8 and Sentinel-1 data. Remote Sens. Environ., 216, 201-211, https://doi.org/10.1016/j.rse.2018.06.044, 2018.

Beck, H. E., Zimmermann, N. E., Mcvicar, T. R., Vergopolan, N., and Wood, E. F.: Present and future kppen-geiger climate classification maps at 1-km resolution. Scientific Data, 5, 180214. https://doi.org/10.1038/sdata.2018.214, 2018.

Boardman, J.W.: Automating spectral unmixing of aviris data using convex geometry concepts. In, Jpl Airborne Geoscience Workshop. 2013.

Bradley, J.V.: Distribution-Free Statistical Test. Englewood Cliffs: Prentice-Hall, 1968.

Chasek, P., Mariam, A.S., Orr, B. J., Luise, A., Ratsimba, H. R., Safriel, U.: Land degradation neutrality: the science-policy interface from the UNCCD to national implementation. Environmental science & policy, 92, 182-190, https://doi.org/10.1016/j.envsci.2018.11.017.

https://doi.org/10.5194/essd-2023-341
Preprint. Discussion started: 10 October 2023

Chen, C., Park, T., Wang, X., Piao, S., Xu, B., Chaturvedi, R.K., Fuchs, R., Brovkin, V., Ciais, P., Fensholt, R.: China and India lead in greening of the world through land-use management. Nature Sustainability, 2, 122-129, https://doi.org/10.1038/s41893-019-0220-7, 2019

Clarke, K.D., Okin, G.S., Lewis, M.M.: Comparison of methods for estimation of absolute vegetation and soil fractional cover using MODIS normalized BRDF-adjusted reflectance data. Remote Sens. Environ., 130, 266-279, https://doi.org/10.1016/j.rse.2012.11.021, 2013

Daldegan, G.A., Roberts, D.A., Ribeiro, F.: Spectral mixture analysis in Google Earth Engine to model and delineate fire scars over a large extent and a long time-series in a rainforest-savanna transition zone. Remote Sens. Environ., 232, 111340. https://doi.org/10.1016/j.rse.2019.111340, 2019

DiMiceli, C., Carroll, M., Sohlberg, R., Kim, D., Kelly, M., Townshend, J.: MOD44B MODIS/Terra Vegetation Continuous Fields Yearly L3 Global 250m SIN Grid V006. In: NASA EOSDIS Land Processes DAAC, 2015.

Elmore, A.J., Mustard, J.F., Manning, S.J., Lobell, D.B.: Quantifying vegetation change in semiarid environments: Precision and accuracy of spectral mixture analysis and the normalized difference vegetation index. Remote Sens. Environ., 73, 87-102, https://doi.org/10.1016/S0034-4257(00)00100-0, 2000

Friedl, M. and Sulla-Menashe, D. MCD12Q1 MODIS/Terra+Aqua Land Cover Type Yearly L3 Global 500m SIN Grid V006.: NASA EOSDIS Land Processes DAAC, 2015.

Franke, J., Roberts, D.A., Halligan, K., Menz, G.: Hierarchical Multiple Endmember Spectral Mixture Analysis (MESMA) of hyperspectral imagery for urban environments. Remote Sens. Environ., 113, 1712-1723, https://doi.org/10.1016/j.rse.2009.03.018, 2022.

Heinz, D.C., Chein-I-Chang: Fully constrained least squares linear spectral mixture analysis method for material quantification in hyperspectral imagery. IEEE Transactions on Geoscience & Remote Sensing, 39, 529-545 , https://doi.org/10.1109/36.911111, 2002.

Hirsch, R.M., Slack, J.R., Smith, R.A.: Techniques of trend analysis for monthly water quality data. Water Resour. Res., 18, 107-121, https://doi.org/10.1029/WR018i001p00107, 1982.

Hugonnet, R., Mcnabb, R., Berthier, E., Menounos, B., Kb, A.: Accelerated global glacier mass loss in the early twenty-first century. Nature, 592, 726-731, https://doi.org/10.1038/s41586-021-03436-z, 2021.

IPCC: Climate Change 2013: The Physical Science Basis. 2013

Kendall, M.G. 1975. Rank correlation methods. London: Charles Griffin

Kuang, W., Du, G., Lu, D., Dou, Y., Miao, C.: Global observation of urban expansion and land-cover dynamics using satellite big-data. Sci Bull, 66, 297-300, https://doi.org/10.1016/j.scib.2020.10.022, 2020.

Kuang, W., Zhang, S., Li, X., Lu, D.: A 30 m resolution dataset of china's urban impervious surface area and green space, 2000-2018. Earth System Science Data, 13. 63–82, https://doi.org/10.5194/essd-13-63-2021, 2021.

Lawrence, D., Vandecar, K.: Effects of tropical deforestation on climate and agriculture. Nat Clim Change, 5, 27-36, https://doi.org/10.1038/nclimate2430, 2015.

Lewińska, K. E., Hostert, P., Buchner, J., Bleyhl, B., Radeloff, V. C.: Short-term vegetation loss versus decadal degradation of grasslands in the Caucasus based on Cumulative Endmember Fractions. Remote Sens. Environ., 248, 111969. https://doi.org/10.1016/j.rse.2020.111969, 2020.

Liu, H., Gong, P., Wang, J., Clinton, N., Bai, Y., and Liang, S.: Annual dynamics of global land cover and its long-term changes from 1982 to 2015, Earth Syst. Sci. Data, 12, 1217–1243, https://doi.org/10.5194/essd-12-1217-2020, 2020.

Liu, X., Huang, Y., Xu, X., Li, X., Zeng, Z.: High-spatiotemporal-resolution mapping of global urban change from 1985 to 2015. Nature Sustainability, 564-570, https://doi.org/10.1038/s41893-020-0521-x, 2020.

Mann, H.B.: Nonparametric tests against trend. Econometrica: Journal of the econometric society, 245-259, https://doi.org/10.2307/1907187, 1945.

Meyer, T., Okin, G.S.: Evaluation of spectral unmixing techniques using MODIS in a structurally complex savanna environment for retrieval of green vegetation, nonphotosynthetic vegetation, and soil fractional cover. Remote Sens. Environ., 161, 122-130, https://doi.org/10.1016/j.rse.2015.02.013, 2015.

Okin, G.S.: Relative spectral mixture analysis — A multitemporal index of total vegetation cover. Remote Sens. Environ., 106, 467-479, https://doi.org/10.1016/j.rse.2006.09.018, 2007.

Olofsson, P., Stehman, S.V., Woodcock, C.E., Sulla-Menashe, D., Sibley, A.M., Newell, J.D., Friedl, M.A., Herold, M.: A global land-cover validation data set, part I: Fundamental design principles. Int. J. Remote Sens., 33, 5768-5788, https://doi.org/10.1080/01431161.2012.674230,2012.

Pengra, B., Long, J., Dahal, D., Stehman, S.V., Loveland, T.R.: A global reference database from very high resolution commercial satellite data and methodology for application to Landsat derived 30 m continuous field tree cover data. Remote Sens. Environ., 165, 234-248, https://doi.org/10.1016/j.rse.2015.01.018, 2015

Piao, S., Friedlingstein, P., Ciais, P., Zhou, L., Chen, A.: Effect of climate and CO2 changes on the greening of the Northern Hemisphere over the past two decades. Geophys. Res. Lett., 33, L23402, https://doi.org/10.1029/2006GL028205, 2006.

https://doi.org/10.5194/essd-2023-341
Preprint. Discussion started: 10 October 2023

Qin, Y., Xiao, X., Dong, J., Zhang, Y., Wu, X., Shimabukuro, Y., Arai, E., Biradar, C., Wang, J., Zou, Z.: Improved estimates of forest cover and loss in the Brazilian Amazon in 2000–2017. Nature Sustainability, 2, 764-772, https://doi.org/10.1038/s41893-019-0336-9, 2019.

Qin, Y., Xiao, X., Wigneron, J., Ciais, P., Brandt, M., Fan, L., Li, X., Crowell, S., Wu, X., Doughty, R.: Carbon loss from forest degradation exceeds that from deforestation in the Brazilian Amazon. Nat Clim Change, 11, 442-448, https://doi.org/10.1038/s41558-021-01026-5, 2021.

Rashed, T., Weeks, J.R., Roberts, D., Rogan, J., Powell, R.: Measuring the physical composition of urban morphology using multiple endmember spectral mixture models. Photogrammetric Engineering & Remote Sensing, 69, 1011-1020, https://doi.org/10.14358/PERS.69.9.1011, 2003

Réjou-Méchain, M., Mortier, F., Bastin, J., Cornu, G., Barbier, N., Bayol, N., Bénédet, F., Bry, X., Dauby, G., Deblauwe, V.: Unveiling African rainforest composition and vulnerability to global change. Nature, 593, 90-94, https://doi.org/10.1038/s41586-021-03483-6, 2021.

Roberts, D.A., Smith, M.O., Adams, J.B.: Green vegetation, nonphotosynthetic vegetation, and soils in AVIRIS data. Remote Sens. Environ., 44, 255-269, https://doi.org/10.1016/0034-4257(93)90020-X, 1993.

Roberts, D.A., Gardner, M., Church, R., Ustin, S., Scheer, G., Green, R.O.: Mapping Chaparral in the Santa Monica Mountains Using Multiple Endmember Spectral Mixture Models. Remote Sens. Environ., 65, 267-279, https://doi.org/10.1016/S0034-4257(98)00037-6, 1998.

Rogan, J., Franklin, J., Roberts, D.A.: A comparison of methods for monitoring multitemporal vegetation change using Thematic Mapper imagery. Remote Sens. Environ., 80, 143-156, https://doi.org/10.1016/S0034-4257(01)00296-6. 2002.

Schaaf, C., Wang, Z.: MCD43A4 MODIS/Terra+Aqua BRDF/Albedo Nadir BRDF Adjusted Ref Daily L3 Global - 500m V006. In: NASA EOSDIS Land Processes DAAC

Sen, Kumar, P.: Estimates of the Regression Coefficient Based on Kendall's Tau. Publications of the American Statistical Association, 63, 1379-1389, https://doi.org/10.1080/01621459.1968.10480934, 1968.

Small, C.: The Landsat ETM+ spectral mixing space. Remote Sens. Environ., 93, 1-17, https://doi.org/10.1016/j.rse.2004.06.007, 2004

Small, C., Milesi, C.: Multi-scale standardized spectral mixture models. Remote Sens. Environ., 136, 442-454, https://doi.org/10.1016/j.rse.2013.05.024, 2013.

Smith, A.M.S., Drake, N.A., Woosterj, M.J., Hudak, A.T., Holden, Z.A., Gibbons, C.J.: Production of Landsat ETM+ reference imagery of burned areas within Southern African savannahs: comparison of methods and application to MODIS. Int. J. Remote Sens., 28, 2753-2775, https://doi.org/10.1016/10.1080/01431160600954704, 2007.

https://doi.org/10.5194/essd-2023-341
Preprint. Discussion started: 10 October 2023

Smith, M.O., Ustin, S.L., Adams, J.B., Gillespie, A.R.: Vegetation in deserts: I. A regional measure of abundance from multispectral images. Remote Sens. Environ., 31, 1-26, https://doi.org/10.1016/0034-4257(90)90074-V, 1990.

Smith, W.K., Dannenberg, M.P., Yan, D., Herrmann, S., Barnes, M. L., Barron-Gafford, G.A., Biederman, J. A, Ferrenberg, S., Fox, A.M., Hudson, A., Knowles, J.F., MacBean, N., Moore, D.J.P., Nagler, P.L., Reed S. C., Rutherford, W.A., Scott, R. L., Wang, X., Yang, J.: Remote sensing of dryland ecosystem structure and function: Progress, challenges, and opportunities. Remote Sens. Environ., 233, 111401, https://doi.org/10.1016/j.rse.2019.111401, 2019.

Soheb, M., Ramanathan, A., Bhardwaj, A., Coleman, M., Rea, B. R., Spagnolo, M., Singh, S., and Sam, L.: Multitemporal glacier inventory revealing four decades of glacier changes in the Ladakh region, Earth Syst. Sci. Data, 14, 4171–4185, doi: 10.5194/essd-14-4171-2022, 2022.

Song, X., Hansen, M.C., Stehman, S.V., Potapov, P.V., Tyukavina, A., Vermote, E.F., Townshend, J.R.: Global land change from 1982 to 2016. Nature, 560, 639-643, https://doi.org/10.1038/s41586-018-0411-9, 2018.

Sonnentag, O., Chen, J.M., Roberts, D.A., Talbot, J., Halligan, K.Q., Govind, A.: Mapping tree and shrub leaf area indices in an ombrotrophic peatland through multiple endmember spectral unmixing. Remote Sens. Environ., 109, 342-360, https://doi.org/10.1016/j.rse.2007.01.010, 2007.

Sousa, D., Small, C.: Globally standardized MODIS spectral mixture models. Remote Sens Lett, 10, 1018-1027, https://doi.org/10.1080/2150704X.2019.1634299, 2019

Sousa, D., Small, C.: Spectral mixture analysis as a unified framework for the remote sensing of evapotranspiration. Remote Sensing, 10(12), 1961, https://doi.org /10.3390/rs10121961, 2018.

Stehman, S.V., Olofsson, P., Woodcock, C.E., Herold, M., Friedl, M.A.: A global land-cover validation data set, II: Augmenting a stratified sampling design to estimate accuracy by region and land-cover class. Int. J. Remote Sens., 33, 6975-6993, https://doi.org/10.1080/01431161.2012.695092, 2012

Sun, D.: Detection of dryland degradation using Landsat spectral unmixing remote sensing with syndrome concept in Minqin County, China. International Journal of Applied Earth Observation & Geoinformation, 41, 34-45, https://doi.org/10.1016/j.jag.2015.04.015, 2015.

Sun, D., Zhang, P., Sun, Q., Jiang, W.: A dryland cover state mapping using catastrophe model in a spectral endmember space of OLI: a case study in Minqin, China. Int. J. Remote Sens., 1-22, https://doi.org/10.1080/01431161.2019.1580795, 2019.

Sun, Q.: A global estimate of monthly vegetation and soil fractions from spatio-temporally adaptive spectral mixture analysis during 2001-2011. https://doi.org/10.5281/zenodo.8323292, 2023a.

Sun, Q.: A global estimate of monthly vegetation and soil fractions from spatio-temporally adaptive spectral mixture analysis during 2012-2022. https://doi.org/10.5281/zenodo.8331843, 2023b.

https://doi.org/10.5194/essd-2023-341
Preprint. Discussion started: 10 October 2023

Sun, Q., Zhang, P., Sun, D., Liu, A., Dai, J.: Desert vegetation-habitat complexes mapping using Gaofen-1 WFV (wide field of view) time series images in Minqin County, China. Int J. Appl Earth Obs, 73, 522-534, https://doi.org/10.1016/j.jag.2018.07.021, 2018.

Sun, Q., Zhang, P., Wei, H., Liu, A., You, S., Sun, D.: Improved mapping and understanding of desert vegetation-habitat complexes from intraannual series of spectral endmember space using cross-wavelet transform and logistic regression. Remote Sens. Environ., 236, 111516. https://doi.org/10.1016/j.rse.2019.111516, 2020.

Sun, Q., Zhang, P., Jiao, X., Han, W., Sun, Y., Sun, D.: Identifying and understanding alternative states of dryland landscape: a hierarchical analysis of time series of fractional vegetation-soil nexuses in China's Hexi Corridor. Landscape and urban planning. 215,104225, https://doi.org/10.1016/j.landurbplan.2021.104225, 2021.

Sun, Q., Zhang, P., Jiao, X., Lun, F., Dong, S., Lin, X., Li, X., Sun, D.: A Remotely Sensed Framework for Spatially-Detailed Dryland Soil Organic Matter Mapping: Coupled Cross-Wavelet Transform with Fractional Vegetation and Soil-Related Endmember Time Series. Remote Sens. 14, 1701. https://doi.org/10.3390/rs14071701, 2022.

Suess, S., van der Linden, S., Okujeni, A., Griffiths, P., Leitão, P. J., Schwieder, M., & Hostert, P.: Characterizing 32 years of shrub cover dynamics in southern Portugal using annual Landsat composites and machine learning regression modeling. Remote Sens. Environ. 219, 353-364, https://doi.org/10.1016/j.rse.2018.10.004, 2018.

Tong, X., Brandt, M., Yue, Y., Horion, S., Wang, K., De Keersmaecker, W., Tian, F., Schurgers, G., Xiao, X., Luo, Y., Chen, C., Myneni, R., Shi, Z., Chen, H., Fensholt, R. 2018. Increased vegetation growth and carbon stock in China karst via ecological engineering. Nature Sustainability, 1, 44-50, https://doi.org/10.1038/s41893-017-0004-x, 2021

Wang, Q., Ding, X., Tong, X., Atkinson, P. M.: Spatio-temporal spectral unmixing of time-series images. Remote Sens. Environ., 259, 112407,

Yu, Z., Jin, X., Miao, L., and Yang, X.: A historical reconstruction of cropland in China from 1900 to 2016, Earth Syst. Sci. Data, 13, 3203–3218, doi:10.5194/essd-13-3203-2021, 2021.

Zemp, M., Huss, M., Thibert, E., Eckert, N., Mcnabb, R., Huber, J., Barandun, M., Machguth, H., Nussbaumer, S.U., Gärtner-Roer, I.: Global glacier mass changes and their contributions to sea-level rise from 1961 to 2016. Nature, 568, 382-386, https://doi.org/10.1038/s41586-019-1071-0, 2019.

Zhang, C., Ma, L., Chen, J., Rao, Y., and Chen, X.: Assessing the impact of endmember variability on linear spectral mixture analysis (LSMA): a theoretical and simulation analysis. Remote Sens. Environ., 235, 111471. https://doi.org/10.1016/j.rse.2019.111471, 2019.

https://doi.org/10.5194/essd-2023-341
Preprint. Discussion started: 10 October 2023

Zhang, X., Liu, L., Zhao, T., Gao, Y., Chen, X., Mi, J.: GISD30: global 30 m impervious-surface dynamic dataset from 1985 to 2020 using time-series Landsat imagery on the Google Earth Engine platform, Earth Syst. Sci. Data, 14, 1831–1856, https://doi.org/10.5194/essd-14-1831-2022, 2022.

620 Zhao, M., Cheng, C., Zhou, Y., Li, X., Shen, S., and Song, C.: A global dataset of annual urban extents (1992–2020) from harmonized nighttime lights, Earth Syst. Sci. Data, 14, 517–534, https://doi.org/10.5194/essd-14-517-2022, 2022.

Zhu, Z., Piao, S., Myneni, R.B., Huang, M., Zeng, Z., Canadell, J.G., Ciais, P., Sitch, S., Friedlingstein, P., Arneth, A.: Greening of the Earth and its drivers. Nat Clim Change, 6, 791-795, https://doi.org/10.1038/nclimate3004, 2016